Dynamic theory of nanophotonic control of two-dimensional semiconductor nonlinearities

S. Guazzotti,[1,*] A. Pusch,[1,2] D. E. Reiter,[1,3] and O. Hess[1,†]

[1]*The Blackett Laboratory, Imperial College London, Prince Consort Road, London SW7 2AZ, United Kingdom*
[2]*School of Photovoltaic and Renewable Energy Engineering, UNSW Sydney, 2052 Kensington, Sydney, Australia*
[3]*Institut für Festkörpertheorie, Universität Münster, Wilhelm-Klemm-Str. 10, 48149 Münster, Germany*

(Received 10 April 2018; revised manuscript received 3 November 2018; published 17 December 2018)

We introduce a Maxwell-Bloch simulation approach which self-consistently combines a microscopic description of the carrier and polarization dynamics of a transition-metal-dichalcogenide (TMDC) monolayer with a spatiotemporal full-wave time-domain simulation of Maxwell's equations on the basis of a finite-difference time-domain (FDTD) method beyond the slowly varying amplitude or paraxial approximations. This offers a platform to realistically model, in particular, the typical ultrafast optical excitation experiments in micro- and nanocavities. Our simulations confirm that the weak screening of the Coulomb interaction in TMDC monolayers yields pronounced exciton lines in the linear spectrum and we uncover the second-order nonlinearity represented in the semiconductor Maxwell-Bloch equations by an intraband dipole moment. This allows us to calculate the spectral shape of the exceptionally strong second-harmonic generation around the exciton lines of TMDC monolayers. We demonstrate that the second-harmonic signal can remarkably be further enhanced by several orders of magnitude through a suitably designed (one-dimensional) photonic microcavity. Due to its self-consistency, flexibility, explicit spatio-temporal resolution on the nanoscale and the ready access to light field and electron dynamics, our theory and computational approach is an ideal platform to design and explore spatiotemporal nonlinear and quantum dynamics in complex photonic or plasmonic micro- and nanostructures for optoelectronic, nanophotonic and quantum applications of TMDC monolayers.

DOI: 10.1103/PhysRevB.98.245307

I. INTRODUCTION

When reduced to a single monolayer, transition-metal-dichalcogenides (TMDCs) like MoS_2, $MoSe_2$, or WSe_2 become direct band gap semiconductors [1,2]. Not surprisingly, the prospect of optical control of a TMDC monolayer together with its ultrathin structure has lead to numerous ideas for applications of TMDC monolayers [3] ranging from photodetectors [4–6] to single-photon sources [7–10]. An important property of a TMDC monolayer is of course its linear and nonlinear optical response. In the linear regime, it shows two pronounced exciton lines with the screening leading to exceptionally high exciton binding energies compared to conventional semiconductors [11–15]. In the nonlinear regime, TMDC monolayers exhibit a strong second-harmonic generation (SHG) contribution [16–21] because of the broken inversion symmetry. This is different compared to centrosymmetric systems such as graphene [22] or TMDC bilayers [21,23] where the SHG is suppressed. Due to the weak van der Waals forces between different layers of TMDCs, it is easily possible to combine TMDC monolayers of different materials to form van der Waals heterostructures [24]. Hybrid structures of TMDC monolayers combined with plasmonic structures [25–27] or a photonic structure [28–32] can lead to a strong enhancement of the optical properties or even strong coupling [33]. Clearly, the nano- and microstructured environment qualitatively alters the nonlinear optical response of the TMDC material, yet little is known about the underlying processes and how to meaningfully model this interplay.

Indeed, one needs to understand both the electronic and the optical properties of the materials and the structure. The nonlinear optical response of semiconductor nanostructures calls for a microscopic treatment of the carrier dynamics, while the simulation of the light field in photonic structures requires an adequate description that accounts for the different materials on the nanoscale. Here, we present a practical method combining a microscopic description of the TMDC semiconductor using the many-body semiconductor Bloch equations with a self-consistent spatiotemporal full time-domain simulation of the optical fields beyond the slowly varying amplitude or paraxial approximations on the basis of a finite difference time domain (FDTD) method [34–37] to calculate linear and nonlinear optical signals of a TMDC monolayer embedded in a nanophotonic structure.

We discuss the absorption spectra of a TMDC monolayer exhibiting exciton peaks and relate them to the underlying band structure. As an exemplary material of a typical TMDC, let us in the following focus on MoS_2. When the TMDC monolayer is put on a substrate, the optical properties can change significantly [11,38,39] due to a modification of the screening. We consider different material substrates with different refractive indices and discuss the resulting absorption spectra. Our method is capable of calculating nonlinear optical signals, e.g., thirdharmonic generation [36]. By introducing a permanent dipole, we extend the Bloch equations to also be able to describe the generation of even harmonics. We

*s.guazzotti14@imperial.ac.uk
†o.hess@imperial.ac.uk

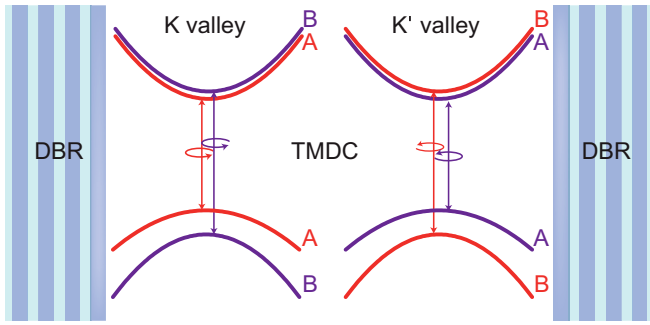

FIG. 1. Sketch of the band structure of a TMDC monolayer. The TMDC monolayer can be embedded into a photonic cavity as indicated by the DBR mirrors at the sides.

focus on SHG, which is particularly strong when the exciting frequency matches half the exciton energy. We demonstrate that by integrating the monolayer in a nanophotonic cavity, the strength of the SHG can be enhanced by several orders of magnitude. Our method provides a versatile tool to simulate possible optoelectronic applications using TMDC monolayers.

II. FULL-WAVE TMDC MAXWELL-BLOCH FRAMEWORK

In our simulations, we model the light field dynamics on the basis of the (spatiotemporal) full-wave time domain Maxwell equations (avoiding the slowly varying amplitude or paraxial approximations) using a FDTD method, coupled self-consistently with a microscopic semiconductor Bloch model for the TMDC monolayer. The FDTD platform is a well-established method used to solve the Maxwell equations for the electric field $\mathbf{E}(\mathbf{r},t)$ and the magnetizing field $\mathbf{H}(\mathbf{r},t)$ in matter via

$$\partial_t \mathbf{H}(\mathbf{r},t) = -\nabla \times \mathbf{E}(\mathbf{r},t)\,, \tag{1a}$$

$$\partial_t \mathbf{E}(\mathbf{r},t) = \frac{1}{\epsilon_b(\mathbf{r})}[\nabla \times \mathbf{H}(\mathbf{r},t) - \partial_t \mathbf{P}(\mathbf{r},t)], \tag{1b}$$

with $\partial_t = \partial/\partial t$ the partial time derivative. The coupling of the field to matter enters via the space-dependent dielectric constant $\epsilon_b(\mathbf{r})$ and via the polarization $\mathbf{P}(\mathbf{r},t)$. We assume a configuration where the TMDC monolayer lies in the xy plane located at z_T and the light field propagates perpendicular to the TMDC monolayer, i.e., in z direction. This simplifies the field dependencies to $\mathbf{E}(z,t)$ and $\mathbf{H}(z,t)$. At the plane of the TMDC, the polarization is $\mathbf{P}(z_T,t)$. Other (inactive) materials enter in the calculation via their dielectric function $\epsilon_b(\mathbf{r})$, which for layered structures reduces to $\epsilon_b(z)$. This enables us to simulate photonic structures, e.g., photonic cavities, which we then combine with the TMDC as indicated in Fig. 1.

To calculate the polarization $\mathbf{P}(z_T,t)$ induced by the TMDC monolayer, we apply a microscopic semiconductor model following Ref. [40]. At the K and K' valley, we take into account four bands each, two conduction and two valence bands. As a consequence of the strong spin-orbit interaction, the valence (conduction) bands are spin-split by Δ_v (Δ_c) at the band edge. The two valleys differ in the arrangement of the bands, e.g., while for the K valley the spin-up band is the uppermost valence band, it is the other way around for the K' valley. We call the bands A and B, adopting the notation of the two excitons used later. A sketch of the band structure is given in Fig. 1. The corresponding Hamiltonian describing the band structure using the electron (hole) creation and annihilation operators $\hat{c}^\dagger_{n,\mathbf{k}}$ ($\hat{d}^\dagger_{n,\mathbf{k}}$) and $\hat{c}_{n,\mathbf{k}}$ ($\hat{d}_{n,\mathbf{k}}$) reads

$$\hat{H}_0 = \sum_{n,\mathbf{k}} \varepsilon^e_n \hat{c}^\dagger_{n,\mathbf{k}} \hat{c}_{n,\mathbf{k}} + \varepsilon^h_n \hat{d}^\dagger_{n,\mathbf{k}} \hat{d}_{n,\mathbf{k}}\,. \tag{2}$$

The dependency of the state on the valleys (K and K') and different bands (A and B) is summarized in the index $n \in \{KA, KB, K'A, K'B\}$. The energies of the states are $\varepsilon^{e/h}_n = \hbar^2\mathbf{k}^2/2m^{e/h}_n + E^{e/h}_n$ with $m^{e/h}_n$ being the effective masses. $E^{e/h}_n$ are the energies at the band edges and $\mathbf{k} = (k_x, k_y, 0)$ is the two-dimensional wave vector. The conduction bands and the valence bands are split by $\Delta^{c/v}$, respectively, and we define the energy difference between the A bands as $E_A = E^e_{KA} - E^h_{KA} = E^e_{K'A} - E^h_{K'A}$ and E_B analogously.

The coupling to the light field is treated in dipole approximation. Only the light field at the TMDC monolayer $\mathbf{E}(z_T,t)$ acts on the semiconductor sheet via the Hamiltonian

$$\hat{H}_{c-l} = \sum_{n,\mathbf{k}} \mathbf{E}(z_T,t) \cdot \left[\mathbf{M}^{cv}_n \hat{c}^\dagger_{n,\mathbf{k}} \hat{d}^\dagger_{n,-\mathbf{k}} + \mathbf{M}^{cv*}_n \hat{d}_{n,-\mathbf{k}} \hat{c}_{n,\mathbf{k}}\right]. \tag{3}$$

The optical selection rules are described by the dipole matrix element $\mathbf{M}^{cv}_n$, which couples the valence band to the conduction band within the same valley and the same type of band (e.g., $KA \to KA$) as marked in Fig. 1. The transitions are circularly polarized with σ^+ polarized transitions in the K valley and σ^- polarized transitions in the K' valley [40]. To account for the polarization-dependent coupling, we use $\mathbf{M}_{KA} = (M_x, iM_y, 0)$ and $\mathbf{M}_{K'A} = (M_x, -iM_y, 0)$ with real-valued $M_{x/y}$ (analogously for the B transition) and approximate the $\mathbf{k}$ dependence of the dipole matrix element by constants.

The resulting Hamiltonian can be used to describe a generic electronic system with several parabolic valleys and strong spin-orbit interaction, resulting in spin-split bands. In particular, this provides a suitable platform for studying several materials within the broad class of TMDC monolayers as their band structures present the same broad features. The parameters included in the model can then be used to tune specific features of the dynamics and thus the response of a specific TMDC can be recovered. A more in-depth discussion of the parameters of the model is provided in the Appendix, together with the values for a MoS_2 monolayer.

On the basis of the Hamiltonians discussed above, we now proceed to set up the equations of motion for the occupations of the electrons $f^e_{n,\mathbf{k}} = \langle \hat{c}^\dagger_{n,\mathbf{k}} \hat{c}_{n,\mathbf{k}} \rangle$ and of the holes $f^h_{n,\mathbf{k}} = \langle \hat{d}^\dagger_{n,\mathbf{k}} \hat{d}_{n,\mathbf{k}} \rangle$. Although there are, in principle, possibilities for several coherences between different bands, the optical transitions occur only between valence and conduction band states with the same index n [cf. Eq. (3)]. Hence, on this stage it is sufficient to consider the polarization $p_{n,\mathbf{k}} = \langle \hat{d}_{n,-\mathbf{k}} \hat{c}_{n,\mathbf{k}} \rangle$.

Introducing the Rabi frequency $\Omega_n = \mathbf{M}_n^{cv} \cdot \mathbf{E}(z_T, t)/\hbar$, we obtain the TMDC Bloch equations [41,42]:

$$\partial_t f^e_{n,\mathbf{k}} = \partial_t f^h_{n,\mathbf{k}} = i(\Omega_n p^*_{n,\mathbf{k}} - \Omega^*_n p_{n,\mathbf{k}}), \tag{4a}$$

$$\partial_t p_{n,\mathbf{k}} = -\frac{i}{\hbar}\left(\varepsilon^e_n + \varepsilon^h_n\right) p_{n,\mathbf{k}} - \gamma_n p_{n,\mathbf{k}} - i\Omega_n\left(f^e_{n,\mathbf{k}} + f^h_{n,\mathbf{k}} - 1\right). \tag{4b}$$

For numerical reasons, we have introduced a phenomenological dephasing rate γ_n, which leads to a broadening of the spectral lines in the optical response.

From the microscopic polarization $p_{n,\mathbf{k}}$, we can calculate the macroscopic polarization via

$$\mathbf{P}(z_T, t) = \sum_{n,\mathbf{k}} \left(p^*_{n,\mathbf{k}} \mathbf{M}^{cv}_n + p_{n,\mathbf{k}} \mathbf{M}^{cv*}_n\right). \tag{5}$$

Note that the macroscopic polarization is a real-valued quantity, although the microscopic polarization and the dipole moment are complex valued. This is an important aspect, because the FDTD simulation is performed with real-valued fields **E** and **H**. The optical polarization now acts back on the fields entering the FDTD simulation [cf. Eq. (1b)] and opens up the possibility to calculate linear and nonlinear optical signals.

III. EXCITONS

To theoretically grasp and model excitonic effects on the microscopic level, we have to include Coulomb interactions in our model and simulation. Indeed, in TMDC monolayers, the weak screening of the Coulomb interaction results in extraordinarily high exciton binding energies [11–14]. Using the standard Coulomb interaction Hamiltonian,

$$H_{c-c} = \frac{1}{2}\sum_{n,\mathbf{k},\mathbf{k}',\mathbf{q}} [V_\mathbf{q} \hat{c}^\dagger_{n,\mathbf{k}+\mathbf{q}} \hat{c}^\dagger_{n,\mathbf{k}'-\mathbf{q}} \hat{c}_{n,\mathbf{k}'} \hat{c}_{n,\mathbf{k}} + V_\mathbf{q} \hat{d}^\dagger_{n,\mathbf{k}+\mathbf{q}} \hat{d}^\dagger_{n,\mathbf{k}'-\mathbf{q}} \hat{d}_{n,\mathbf{k}'} \hat{d}_{n,\mathbf{k}} - 2V_\mathbf{q} \hat{c}^\dagger_{n,\mathbf{k}+\mathbf{q}} \hat{d}^\dagger_{n,\mathbf{k}'-\mathbf{q}} \hat{d}_{n,\mathbf{k}'} \hat{c}_{n,\mathbf{k}}], \tag{6}$$

we describe electron-electron, hole-hole, and electron-hole interactions. The Coulomb interactions lead to a coupling of the different **k** states, which otherwise would be just an ensemble of uncoupled two-level systems [cf. Eq. (4)] [36]. In the following, we shall focus on interactions within the same band which dominate for small densities and truncate the infinite hierarchy of equations on the mean-field level. However, the extension of our model to include intervalley Coulomb scattering is straightforward to, e.g., study intervalley dynamics using two-pulse pump-probe experiments [43,44] and we emphasize that other interaction mechanisms, e.g., electron-phonon interaction, can likewise be included on the microscopic level.

For the TMDC monolayer, we use the two-dimensional Coulomb coupling matrix element $V_\mathbf{q}$ [40]:

$$V_\mathbf{q} = \frac{e^2}{\epsilon_0 \epsilon_s A} \frac{1}{q(1 + r_0 q)}, \tag{7}$$

where e is the elementary charge, ϵ_0 the dielectric constant and A the area. The screening length is given by $r_0 = d\epsilon_\perp/\epsilon_s$ with the inplane dielectric constant $\epsilon_\perp$ and the thickness d of the TMDC monolayer. The dielectric constant ε_s accounts for screening from the environment

$$\epsilon_s = \epsilon_{\text{super}} + \epsilon_{\text{sub}}, \tag{8}$$

which is the sum of the dielectric constants of the substrate ϵ_{sub} and the superstrate ϵ_{super}. Indeed, it was found that the exciton binding energy depends sensitively on the surrounding material [11,38].

Now we calculate the linear optical response for a MoS_2 monolayer with the material parameters given in the Appendix. We send a weak pulse from one side onto the structure, e.g., a freestanding TMDC monolayer or a more sophisticated photonic structure with an embedded TMDC monolayer. The light pulse then propagates through the structure and interacts with the TMDC monolayer. We record the reflected and transmitted fields through the intensities I_{refl} and I_{trans}, respectively [36]. The spectrum α is then calculated via

$$\alpha = 1 - \frac{I_{\text{refl}} + I_{\text{trans}}}{I_{\text{inc}}} \tag{9}$$

with I_{inc} the intensity of the incoming pulse. Without loss of generality, let us choose the polarization of the incoming pulse to be right-handed circular polarization, thereby addressing only the K valley (the results are the same for left-handed circular polarization, where only K' excitons would appear).

Before focusing on a more complex scenario and regimes such as nonlinear processes, we first consider the linear response of a freestanding TMDC monolayer shown in Fig. 2(a). The absorption spectrum exhibits two pronounced peaks, which we attribute to the A and B excitons at 1.90 eV and 2.05 eV. These excitons form due to Coulomb interactions. We find binding energies of about 850 meV, due to the weak screening of the Coulomb interaction in these materials. Our values are comparable to theoretical calculations for MoS_2 using density-functional theory (DFT) methods [45–48]. The energetic splitting between the A and B excitons with 0.15 meV reflects mostly the valence band splitting with $\Delta^v = 0.16$ meV (with $\Delta^c = 0$), while a small difference appears due to the different effective masses of the two valence bands. The difference in peak amplitude can be traced back to different band gaps. Due to the high binding energy, we also clearly see the first excited exciton states as smaller peaks at energies of 2.41 eV and 2.56 eV, as well as the second excited state. In our model, the exciton binding energies follow roughly the solution of the 2D Coulomb potential. Study of the exciton series in TMDC monolayers is still a very active research field because strong deviations from the Rydberg series were found [20,47].

Due to its two-dimensionality, the screening of the Coulomb interaction in a monolayer is strongly affected by the surrounding material. The most common case is a monolayer lying on top of a substrate. In Fig. 2(b), we show the absorption spectrum of a MoS_2 monolayer on glass (refractive index 1.50). Again, we see the A and B exciton peaks, but now at 2.15 eV and 2.30 eV, respectively, i.e., about 0.25 eV higher in energy than for the freestanding layer. The energetic shift for both the A and B excitons is the same and a consequence

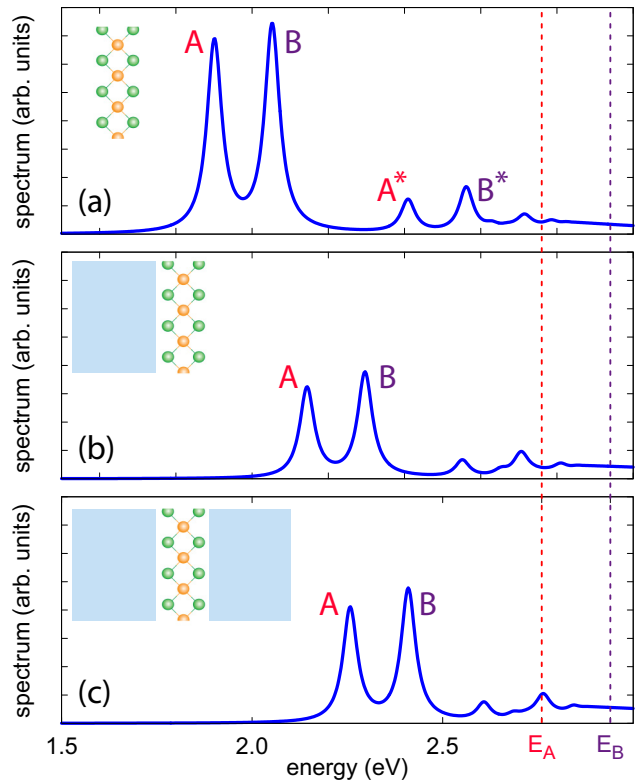

FIG. 2. Absorption spectrum of (a) a freestanding MoS_2 monolayer, (b) a MoS_2 monolayer on glass, and (c) a MoS_2 monolayer sandwiched in glass.

of screening from the substrate. Another element that affects the exciton energy is the renormalization (redshift) of the band gap as reported from DFT calculations [38,49,50] as well as experiments [51]. It has further been shown that the combined effect of binding energy and band-gap renormalization can be used to engineer the position of the excitonic resonances [51,52]. This effect can be accounted for in our simulation by setting the value of the band gap as a substrate dependent parameter.

In a third scenario, we consider the TMDC monolayer sandwiched in glass. The glass superstrate further enhances the screening of the Coulomb interaction and, accordingly, the binding energy of the states is again diminished, resulting in the A and B exciton lines lying at $A = 2.28$ eV and $B = 2.43$ eV. By changing the environment of the TMDC monolayer, one can thus tune the energy of the exciton lines, which is important when embedding a TMDC monolayer into heterostructures.

IV. SECOND-HARMONIC GENERATION

Let us now focus on the nonlinear optical response. In a symmetric material we would *a priori* expect only odd harmonics (like the third, fifth,...harmonics) to be generically generated [36]. Yet SHG was found to be strong in TMDC monolayers and this has been associated with a broken inversion symmetry of the TMDC monolayer lattice [17–20,53], which we microscopically model via the electric field coupling Hamiltonian:

$$\hat{H}_{pd} = -\mathbf{E}(z_T, t) \cdot \sum_{n,\mathbf{k}} \left[\mathbf{M}_n^c \hat{c}_{n,\mathbf{k}}^\dagger \hat{c}_{n,\mathbf{k}} - \mathbf{M}_n^v \hat{d}_{n,\mathbf{k}}^\dagger \hat{d}_{n,\mathbf{k}}\right]. \quad (10)$$

Here, $\mathbf{M}_i^c$ ($\mathbf{M}_i^v$) is the intraband dipole of the conduction (valence) band representing a permanent dipole moment which microscopically models the broken inversion symmetry of the TMDC monolayer lattice. A similar model extending Maxwell-Bloch equations with the inclusion of a permanent dipole has been used in the context of two- and four-level systems to describe the nonlinear response of polarized molecules [54–56]. As the optical excitation takes place perpendicular to the plane, we shall in the following focus on the in-plane components of the intraband dipole moment, which we define as $\mathbf{M}_n^{c/v} = (M_{n,x}^{c/v}, M_{n,y}^{c/v}, 0)$. This is well justified even for a hypothetical nonzero z component, as this component would not couple to the external field with $\mathbf{E}(z_T, t) = (E_x, E_y, 0)$. Indeed, already in the $x-y$ plane the inversion symmetry is broken due to the two-atomic basis in the hexagonal TMDC lattice, i.e., when the system is inverted the metal atom is mirrored on the chalcogenide atom and also the other way around. This is an indication that the in-plane wave functions are also not symmetric, which, in turn, results in an intraband dipole moment. Incidentally, the latter was also shown for tilted quantum wells [57]. Note that the in-plane symmetry can be restored by adding a second TMDC layer, which leads to the second harmonic being suppressed [16,23]. Furthermore, we note that the SHG is polarization dependent, i.e., for a particular symmetry axis the second harmonic is weak [21,23] and for not perfectly aligned stacked TMDC layers strong second-harmonic signals can be found [53,58]. While, for reasons of clarity, we shall in the following assume a $\mathbf{k}$-independent intraband dipole moment, effects such as a polarization-dependent SHG, can in principle be taken into account via a $\mathbf{k}$-dependent matrix element. In our model equations [cf. Eq. (4)] the intraband dipole interaction enters in the equation for the polarization $p_{n,\mathbf{k}}$ via

$$\partial_t p_{n,\mathbf{k}}|_{H_{pd}} = -\frac{i}{\hbar}\mathbf{E}(z_T, t) \cdot \left(\mathbf{M}_n^c - \mathbf{M}_n^v\right) p_{n,\mathbf{k}}\,. \quad (11)$$

Note that the model equations thus now provide the basis for the possibility of a SHG and also higher even harmonics. However, as we consider a dynamic electric field $\mathbf{E}(z_T, t)$, the nonlinear response is obtained directly from the dynamical simulation and consequently fundamental questions such as if SHG is excited at all and with which strength are not predetermined but rather a result of the dynamical simulation.

Let us initially consider the nonlinear optical response of a simple freestanding MoS_2 monolayer. For the optical excitation, we use a sech pulse of the form $E(t) = E_0 \cos(\omega_p t)\mathrm{sech}(t/\tau)$ with linear polarization. The laser pulse excites the system at the energy $\varepsilon_p = \hbar\omega_p$ with a full width at half maximum (FWHM) of the pulse $2\tau \log(2+\sqrt{3}) = 200$ fs. The strength of the pulse is set to $E_0 = 10^8$ V/m. We first set the energy of the laser pulse to half of the A-exciton energy with $\varepsilon_p = 0.95$ eV and calculate the spectrum shown in Fig. 3(a); note that the spectrum is shown on a logarithmic scale. In the spectrum, the most-pronounced peak occurs at the exciting fundamental frequency 0.95 eV being half of

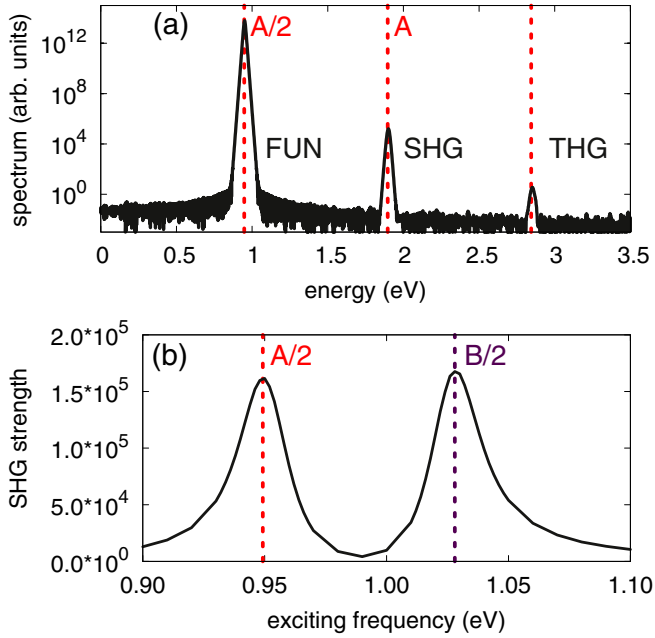

FIG. 3. (a) Nonlinear optical response of a freestanding TMDC monolayer excited by a strong laser pulse showing higher harmonic generation. (b) Strength of the SHG signal as function of the exciting frequency.

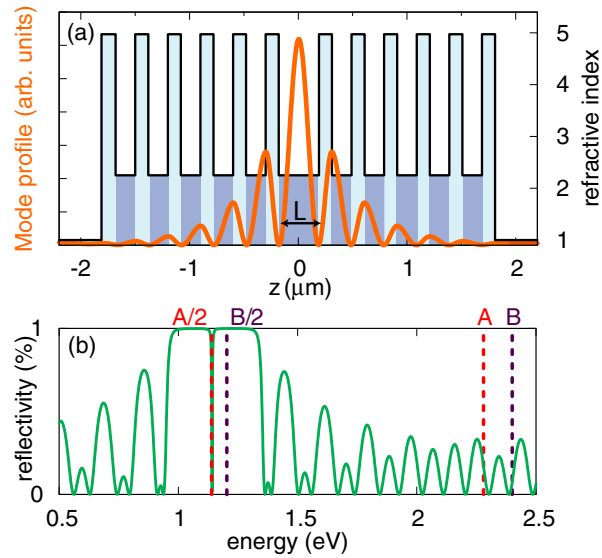

FIG. 4. (a) Sketch of the photonic cavity structure including the refractive index. The mode profile of the fundamental mode is shown in orange. (b) Reflectivity of the cavity. The energies of the A and B excitons in glass as well as half their values are indicated. The cavity mode has a quality factor of $Q \simeq 400$.

the A-exciton energy. Due to higher harmonics generation, we clearly see peaks emerging at multiples of the exciting frequency. The peak at $E = 1.90$ eV constitutes the SHG signal and coincides with the energy of the A-exciton of a freestanding monolayer. The field of the second harmonic is about eight orders of magnitude below the intensity of the fundamental peak. We also see the appearance of the third harmonic at $E = 2.85$ eV. Here, the field is about 13 orders of magnitude lower than the fundamental signal, reflecting the higher order of the process. This is nicely in line with third-harmonic generation having also been experimentally observed in TMDC monolayers [58–60]. We should emphasize that in our "computational experiments," the higher harmonic generation is contained within a full dynamical many-body simulation framework and, in particular, without the explicit use of any terms such as a nonlinear susceptibility. Indeed, in our computational simulations it is the interaction of the light field with the Coulomb-interacting carriers in the semiconductor which leads to the generation of these nonlinear optical signals.

Figure 3(b) shows the dependence of the SHG strength on the fundamental frequency, obtained by sweeping the energy of the exciting laser pulse ε_p between the energies of 0.90 eV and 1.10 eV. Even though the exciton energies are not an explicit input in our calculation, but are rather a result of our computational experiments, we find a strong dependence of the strength of the higher harmonic generation on the exciton energy. We find that at $\varepsilon_p = 0.95$ eV and $\varepsilon_p = 1.03$ eV, the SHG is particularly strong. These energies can be identified with half of the energy of the A and B excitons of the freestanding monolayer, respectively. We conclude that nonlinear processes are much more efficient when a final state for the higher harmonic is present.

To explore a possible enhancement of the nonlinear optical response of a TMDC monolayer, we now embed the TMDC layer into a nanostructured photonic cavity. An important example of such a nanostructured photonic cavity consists of two parallel distributed Bragg mirrors. For specificity, we use a cavity composed of two Bragg mirrors consisting of layers of glass (SiO_2, refractive index 1.50) and silicon nitrite (SiN_x, refractive index 2.23) as shown in Fig. 4(a). Each glass layer is 180-nm thick and each silicon nitride layer is 120-nm thick. The corresponding refractive indices are indicated by the black line in Fig. 4(a). By the periodic arrangement of glass and silicon nitride, a band gap is formed at an energy around 1 eV. In the middle of the layered structure, we thus generate a cavity with an effective length L, such that a confined mode emerges with a quality factor $Q \simeq 400$. An example of a confined mode is shown in Fig. 4(a) (orange color) and the reflectivity is shown in Fig. 4(b). Due to the confinement of the mode, we find a strong field enhancement in the middle of the cavity. By changing the length L of the cavity, we can control the energy of the cavity mode. Figure 5 shows the energy of the cavity mode as function of the cavity length L (green curve). When the cavity length is increased from $L = 250$ nm to $L = 450$ nm, the mode energy decreases from 1.26 eV to 1.07 eV. Because all cavity modes lie well within the stop band of the photonic structure, the change of the cavity mode as function of the cavity length is approximately linear.

Now let us introduce the TMDC monolayer at the field maximum of the cavity and consider the strength of the second-harmonic signal in this new configuration. We adjust the exciting frequency of the impinging laser pulse to match the frequency of the cavity mode and the resulting strength of the SHG is displayed in Fig. 5 (black curve) as function of cavity length. We find that for a cavity length of

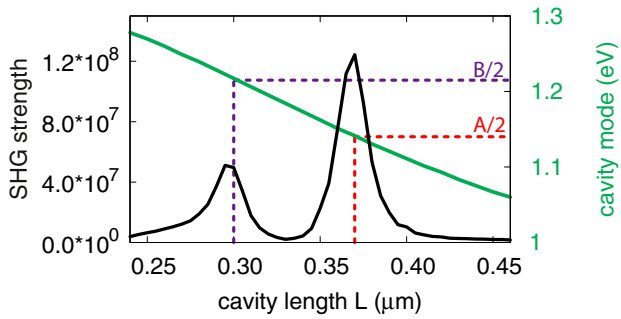

FIG. 5. Green: Energy of the cavity mode (right-hand axis) as a function of cavity length. Black: Intensity of the SHG when the excitation is resonant with the cavity mode (left-hand axis). The dashed red (purple) line identifies the length for which the SHG of the cavity mode is resonant with the A (B) exciton.

300 nm and for 370 nm, a pronounced enhancement occurs. Remarkably, due to the cavity structure, the second-harmonic signal is now up to three orders of magnitude stronger than for the solitary freestanding monolayer. The difference in strength between the two peaks can be explained by the different field strengths of the cavity modes, which directly affects the efficiency of the higher harmonic generation. The pronounced resonances at certain cavity lengths can be traced back to the exciton frequencies of the TMDC monolayer. Here, one has to be careful to use the shifted exciton frequencies due to the modified screening by the surrounding material as shown in Fig. 2(c). Indeed, we find the strongest amplification at the energies 1.14 eV (at $L = 370$ nm) and 1.22 eV (at $L = 300$ nm) being half of the A (2.28 eV) and B (2.43 eV) exciton energies of the monolayer sandwiched in glass [cf. Fig. 2(c)].

V. CONCLUSIONS

In this paper, we have introduced a dynamic full-wave theoretical framework to calculate linear and nonlinear optical signals of photoexcited semiconducting TMDC monolayers embedded in a nanostructured photonic cavity, combining a full-wave spatiotemporal representation of Maxwell's equations (beyond the slowly varying envelope or paraxial approximations) solved on the basis of a FDTD method with many-body semiconductor-Bloch equations for TMDC. Combining a dynamic full-wave and spatially resolved simulation of Maxwell's equations with semiconductor Bloch equations for TMDC materials allows us to track the light field dynamics as well as the electron dynamics. To achieve this description, the TMDC model takes into account all spin and valley indices as well as polarization-dependent selection rules for the coupling to the vectorial fields of the FDTD simulation. Because our method can readily be expanded to include electron-phonon interaction or electron-electron scattering processes, it can further be used to monitor processes like valley-dependent scattering.

Computational experiments performed within this framework confirm that TMDC monolayers show very pronounced excitonic effects (which are taken on board by calculating the Coulomb interaction dynamically on a Hartree-Fock level), as well as a very strong SHG (modelled via consideration of a permanent intraband dipole). The second-order nonlinear response is not an input parameter that we funnel into the model but emerges dynamically from the inherent non-linear structure of the semiconductor Bloch equations. Furthermore, the self-consistent nature of the simulations allows us to theoretically determine the spectral shape of the second-harmonic signal in a MoS_2 monolayer, which peaks very strongly at resonance with the excitons. This is particularly interesting in TMDC materials, where the peaks are separated by several hundreds of meV from the band gap, in contrast to conventional semiconductor quantum wells in which such strong binding energies are not possible.

Moreover, we have demonstrated that the second-harmonic signal of a photoexcited TMDC monolayer can be significantly enhanced by an appropriately designed cavity. Such an enhanced nonlinear interaction can conceivably eliminate the need for phase matching due to the giant SHG in a single TMDC monolayer compared to other previously available quasi-two-dimensional structures such as asymmetric quantum wells. In contrast to conventional semiconductor quantum wells, which are always embedded into other semiconductor materials, TMDCs can be readily combined with other (isolating, semiconducting, or metallic) materials to enhance the light-matter interaction. While we here chose as an example a SiO_2 cavity with (subwavelength structured) distributed Bragg mirrors, an extension to other materials including, in particular, nanoplasmonic cavities and waveguides, is readily possible in our approach thanks to the subwavelength spatial resolution of our full-wave (spatiotemporal) method. Therefore, our method can be employed to calculate the interaction with arbitrary plasmonic structures as well as with photonic crystals in two or three dimensions. It is also possible to include one or more separated TMDC monolayers. Thus, our method constitutes an ideal platform to explore and design nanophotonic structures which employ TMDC monolayers to achieve novel optical functionalities.

ACKNOWLEDGMENTS

We thank Matthias Drüppel, Michael Rohlfing, and Rudolf Bratschitsch for useful discussions. D.E.R. thanks the German Academic Exchange Service (DAAD) for financial support within the P.R.I.M.E. programme. D.E.R. gratefully acknowledges financial support by the Deutsche Forschungsgemeinschaft (DFG) via Project No. RE4183/2-1. This study was partially supported by the Air Force Office of Scientific Research (AFOSR), and support by the European Office of Aerospace Research and Development (EOARD) is also acknowledged. This work was supported by the EPSRC through Grant No. EP/L027151/1.

APPENDIX: MATERIAL PARAMETERS

In this paper, we consider MoS_2 as material with the corresponding parameters listed in Table I. Other TMDC monolayers like WS_2 and WSe_2 can be easily adopted by changing the material parameters. We assume that the conduction band splitting is negligible and only the valence band is split. The band gap E_{gap} is defined such that it lies in the middle of the spin split bands, resulting in band gaps of $E_A = 2.76$ eV and

TABLE I. Parameters of MoS_2 with m_0 being the free electron mass

effective mass electron	m^e	0.480 m_0
effective mass hole A	m_A^v	0.575 m_0
effective mass hole B	m_B^v	0.660 m_0
band gap	E_{gap}	2.84 eV
valence band splitting	Δ_v	160 meV
conduction band splitting	Δ_c	0 meV
dipole matrix element	$\lvert M^{cv}\rvert_x = \lvert M^{cv}\rvert_y$	0.2 nm
intraband dipole	$\lvert M^c - M^v\rvert_{x,y}$	0.02 nm
layer thickness	d	0.312 nm
in-plane dielectric constant	$\varepsilon_\perp$	12
dephasing rate	γ	$1/30\ \text{fs}^{-1}$

$E_B = 2.94$ eV for the A and B bands, respectively. The band structure parameters (effective masses, band energies, and spin-orbit splitting) are taken from Ref. [40] and come from fitting a tight-binding model to a set of DFT band structures. The resulting isotropic valleys provide a low excitation energy approximation to the trigonal-shaped valleys obtained from *a priori* calculations. The combination of conduction and valence band spin-orbit splitting, Δ_c and Δ_v, determines the energy difference between the A and B exciton series. The A (B) exciton binding energy, and thus its spectral position, comes from the effective electron and hole masses, m^c and m_A^v (m_B^v), as well as the specifics of the Coulomb interaction. In particular, the screening from the dielectric environment, $\epsilon_s = \epsilon_{\text{super}} + \epsilon_{\text{sub}}$, provides a scaling of the Coulomb matrix elements, cf. Eq. (7), which results in the renormalization observed in Fig. 2. Conversely, the screening length, $r_0 = d\epsilon_\perp/\epsilon_s = 3.744\,\text{nm}/\epsilon_s$, affects the excitonic series beyond a simple scaling of the binding energies. This produces the experimentally observed nonhydrogenic Rydberg series [11]. The values for the monolayer thickness, d, and the in-plane dielectric constant, $\epsilon_\perp$, can be obtained via DFT simulations of the bulk material, see, e.g., Refs. [12,61]. In the limiting case of $d \to 0$ or $\epsilon_s \to \infty$, this reduces to a 2D hydrogenic Rydberg series, while for $d \to \infty$ it reproduces the 3D result. The dipole matrix elements, $\mathbf{M}^{cv}$, are calculated from the momentum matrix elements in Ref. [40] via $\mathbf{M}_v^{cv} = \hbar\mathbf{p}_v^{cv}/(i\mu_v E_v)$ with the reduced mass, μ_v, the band-gap energies, E_v, and $v \in \{A, B\}$. The intraband dipole, $\mathbf{M}^c - \mathbf{M}^v$, can be determined via a comparison with experimental results of SHG in the chosen material. Lastly, the dephasing rate provides a phenomenological way to introduce broadening of the resonances.

[1] Q. H. Wang, K. Kalantar-Zadeh, A. Kis, J. N. Coleman, and M. S. Strano, Electronics and optoelectronics of two-dimensional transition metal dichalcogenides, Nat. Nanotechnol. **7**, 699 (2012).

[2] A. Kumar and P. K. Ahluwalia, Electronic structure of transition metal dichalcogenides monolayers 1H-MX2 (M= Mo, W; X= S, Se, Te) from *ab-initio* theory: New direct band gap semiconductors, Eur. Phys. J. B **85**, 186 (2012).

[3] K. F. Mak and J. Shan, Photonics and optoelectronics of 2d semiconductor transition metal dichalcogenides, Nat. Photon. **10**, 216 (2016).

[4] O. Lopez-Sanchez, D. Lembke, M. Kayci, A. Radenovic, and A. Kis, Ultrasensitive photodetectors based on monolayer MoS_2, Nat. Nanotechnol. **8**, 497 (2013).

[5] F. H. L. Koppens, T. Mueller, P. Avouris, A. C. Ferrari, M. S. Vitiello, and M. Polini, Photodetectors based on graphene, other two-dimensional materials and hybrid systems, Nat. Nanotechnol. **9**, 780 (2014).

[6] D. B. Velusamy, R. H. Kim, S. Cha, J. Huh, R. Khazaeinezhad, S. H. Kassani, G. Song, S. M. Cho, S. H. Cho, I. Hwang, J. Lee, K. Oh, H. Choi, and C. Park, Flexible transition metal dichalcogenide nanosheets for band-selective photodetection, Nat. Commun. **6**, 8063 (2015).

[7] P. Tonndorf, R. Schmidt, R. Schneider, J. Kern, M. Buscema, G. A. Steele, A. Castellanos-Gomez, H. S. J. van der Zant, S. Michaelis de Vasconcellos, and R. Bratschitsch, Single-photon emission from localized excitons in an atomically thin semiconductor, Optica **2**, 347 (2015).

[8] M. Koperski, K. Nogajewski, A. Arora, V. Cherkez, P. Mallet, J.-Y. Veuillen, J. Marcus, P. Kossacki, and M. Potemski, Single photon emitters in exfoliated WSe_2 structures, Nat. Nanotechnol. **10**, 503 (2015).

[9] Y.-M. He, G. Clark, J. R. Schaibley, M.-C. He, Y. Chen, Y. J. Wei, X. Ding, Q. Zhang, W. Yao, X. Xu, C.-Y. Lu, and J.-W. Pan, Single quantum emitters in monolayer semiconductors, Nat. Nanotechnol. **10**, 497 (2015).

[10] J. Kern, I. Niehues, P. Tonndorf, R. Schmidt, D. Wigger, R. Schneider, T. Stiehm, S. Michaelis de Vasconcellos, D. E. Reiter, T. Kuhn, and R. Bratschitsch, Nanoscale positioning of single-photon emitters in atomically thin WSe_2, Adv. Mater. **28**, 7101 (2016).

[11] A. Chernikov, T. C. Berkelbach, H. M. Hill, A. Rigosi, Y. Li, O. B. Aslan, D. R. Reichman, M. S. Hybertsen, and T. F. Heinz, Exciton Binding Energy and Nonhydrogenic Rydberg Series in Monolayer WS_2, Phys. Rev. Lett. **113**, 076802 (2014).

[12] T. Cheiwchanchamnangij and W. R. L. Lambrecht, Quasiparticle band structure calculation of monolayer, bilayer, and bulk MoS_2, Phys. Rev. B **85**, 205302 (2012).

[13] A. Ramasubramaniam, Large excitonic effects in monolayers of molybdenum and tungsten dichalcogenides, Phys. Rev. B **86**, 115409 (2012).

[14] B. Zhu, X. Chen, and X. Cui, Exciton binding energy of monolayer WS_2, Sci. Rep. **5**, 9218 (2015).

[15] F. Cadiz, E. Courtade, C. Robert, G. Wang, Y. Shen, H. Cai, T. Taniguchi, K. Watanabe, H. Carrere, D. Lagarde, M. Manca, T. Amand, P. Renucci, S. Tongay, X. Marie, and B. Urbaszek, Excitonic Linewidth Approaching the Homogeneous Limit in MoS_2-Based van der Waals Heterostructures, Phys. Rev. X **7**, 021026 (2017).

[16] H. Zeng, G.-B. Liu, J. Dai, Y. Yan, B. Zhu, R. He, L. Xie, S. Xu, X. Chen, W. Yao, and X. Cui, Optical signature of symmetry

variations and spin-valley coupling in atomically thin tungsten dichalcogenides, Sci. Rep. **3**, 1608 (2013).

[17] N. Kumar, S. Najmaei, Q. Cui, F. Ceballos, P. M. Ajayan, J. Lou, and H. Zhao, Second harmonic microscopy of monolayer MoS_2, Phys. Rev. B **87**, 161403 (2013).

[18] L. M. Malard, T. V. Alencar, A. P. M. Barboza, K. F. Mak, and A. M. de Paula, Observation of intense second harmonic generation from MoS_2 atomic crystals, Phys. Rev. B **87**, 201401(R) (2013).

[19] C. Janisch, Y. Wang, D. Ma, N. Mehta, A. L. Elías, N. Perea-López, M. Terrones, V. Crespi, and Z. Liu, Extraordinary second harmonic generation in tungsten disulfide monolayers, Sci. Rep. **4**, 5530 (2014).

[20] G. Wang, X. Marie, I. Gerber, T. Amand, D. Lagarde, L. Bouet, M. Vidal, A. Balocchi, and B. Urbaszek, Giant Enhancement of the Optical Second-Harmonic Emission of WSe_2 Monolayers by Laser Excitation at Exciton Resonances, Phys. Rev. Lett. **114**, 097403 (2015).

[21] K. L. Seyler, J. R. Schaibley, P. Gong, P. Rivera, A. M. Jones, S. Wu, J. Yan, D. G. Mandrus, W. Yao, and X. Xu, Electrical control of second-harmonic generation in a WSe_2 monolayer transistor, Nat. Nanotechnol. **10**, 407 (2015).

[22] M. M. Glazov, Second harmonic generation in graphene, JETP Lett. **93**, 366 (2011).

[23] Y. Li, Y. Rao, K. F. Mak, Y. You, S. Wang, C. R. Dean, and T. F. Heinz, Probing symmetry properties of few-layer MoS_2 and *h*-BN by optical second-harmonic generation, Nano Lett. **13**, 3329 (2013).

[24] A. K. Geim and I. V. Grigorieva, Van der Waals heterostructures, Nature **499**, 419 (2013).

[25] J. Kern, A. Trügler, I. Niehues, J. Ewering, R. Schmidt, R. Schneider, S. Najmaei, A. George, J. Zhang, J. Lou, U. Hohenester, S. Michaelis de Vasconcellos, and R. Bratschitsch, Nanoantenna-enhanced light-matter interaction in atomically thin WS_2, ACS Photonics **2**, 1260 (2015).

[26] X. Li, J. Zhu, and B. Wei, Hybrid nanostructures of metal/two-dimensional nanomaterials for plasmon-enhanced applications, Chem. Soc. Rev. **45**, 3145 (2016).

[27] A. D. Johnson, F. Cheng, Y. Tsai, and C.-K. Shih, Giant enhancement of defect bound exciton luminescence and suppression of band-edge luminescence in monolayer WSe_2-Ag plasmonic hybrid structures, Nano Lett. **17**, 4317 (2017).

[28] A. Majumdar, C. M. Dodson, T. K. Fryett, A. Zhan, S. Buckley, and D. Gerace, Hybrid 2D material nanophotonics: A scalable platform for low-power nonlinear and quantum optics, ACS Photonics **2**, 1160 (2015).

[29] F. Yi, M. Ren, J. C. Reed, H. Zhu, J. Hou, C. H. Naylor, A. T. C. Johnson, R. Agarwal, and E. Cubukcu, Optomechanical enhancement of doubly resonant 2D optical nonlinearity, Nano Lett. **16**, 1631 (2016).

[30] J. K. Day, M.-H. Chung, Y.-H. Lee, and V. M. Menon, Microcavity enhanced second harmonic generation in 2D MoS_2, Opt. Mater. Express **6**, 2360 (2016).

[31] T. K Fryett, K. L Seyler, J. Zheng, C.-H. Liu, X. Xu, and A. Majumdar, Silicon photonic crystal cavity enhanced second-harmonic generation from monolayer WSe_2, 2D Mater. **4**, 015031 (2016).

[32] S. Hammer, H. M. Mangold, A. E. Nguyen, D. Martinez-Ta, S. Naghibi Alvillar, L. Bartels, and H. J. Krenner, Scalable and transfer-free fabrication of MoS_2/SiO_2 hybrid nanophotonic cavity arrays with quality factors exceeding 4000, Sci. Rep. **7**, 7251 (2017).

[33] M.-E. Kleemann, R. Chikkaraddy, E. M. Alexeev, D. Kos, C. Carnegie, W. Deacon, A. C. de Pury, C. Große, B. de Nijs, J. Mertens, A. I. Tartakovskii, and J. J. Baumberg, Strong-coupling of WSe_2 in ultra-compact plasmonic nanocavities at room temperature, Nat. Commun. **8**, 1296 (2017).

[34] K. Böhringer and O. Hess, A full-time-domain approach to spatio-temporal dynamics of semiconductor lasers. I. Theoretical formulation, Progr. Quantum Electron. **32**, 159 (2008).

[35] R. Buschlinger, M. Lorke, and U. Peschel, Light-matter interaction and lasing in semiconductor nanowires: A combined finite-difference time-domain and semiconductor Bloch equation approach, Phys. Rev. B **91**, 045203 (2015).

[36] S. Guazzotti, A. Pusch, D. E. Reiter, and O. Hess, Dynamical calculation of third-harmonic generation in a semiconductor quantum well, Phys. Rev. B **94**, 115303 (2016).

[37] M. Sukharev and A. Nitzan, Optics of exciton-plasmon nanomaterials, J. Phys.: Condens. Matter **29**, 443003 (2017).

[38] Y. Lin, X. Ling, L. Yu, S. Huang, A. L. Hsu, Y.-H. Lee, J. Kong, M. S. Dresselhaus, and T. Palacios, Dielectric screening of excitons and trions in single-layer MoS_2, Nano Lett. **14**, 5569 (2014).

[39] S. Borghardt, J.-S. Tu, F. Winkler, J. Schubert, W. Zander, K. Leosson, and B. E. Kardynał, Engineering of neutral excitons and exciton complexes in transition metal dichalcogenide monolayers through external dielectric screening, Phys. Rev. Mater. **1**, 054001 (2017).

[40] G. Berghäuser and E. Malic, Analytical approach to excitonic properties of MoS_2, Phys. Rev. B **89**, 125309 (2014).

[41] M. Selig, G. Berghäuser, A. Raja, P. Nagler, C. Schüller, T. F. Heinz, T. Korn, A. Chernikov, E. Malic, and A. Knorr, Excitonic linewidth and coherence lifetime in monolayer transition metal dichalcogenides, Nat. Commun. **7**, 13279 (2016).

[42] G. Berghäuser, A. Knorr, and E. Malic, Optical fingerprint of dark 2p-states in transition metal dichalcogenides, 2D Mater. **4**, 015029 (2016).

[43] R. Schmidt, G. Berghaäuser, R. Schneider, M. Selig, P. Tonndorf, E. Malić, A. Knorr, S. Michaelis de Vasconcellos, and R. Bratschitsch, Ultrafast Coulomb-induced intervalley coupling in atomically thin WS_2, Nano Lett. **16**, 2945 (2016).

[44] G. Wang, X. Marie, B. L. Liu, T. Amand, C. Robert, F. Cadiz, P. Renucci, and B. Urbaszek, Control of Exciton Valley Coherence in Transition Metal Dichalcogenide Monolayers, Phys. Rev. Lett. **117**, 187401 (2016).

[45] D. Y. Qiu, F. H. da Jornada, and S. G. Louie, Optical Spectrum of MoS_2 : Many-Body Effects and Diversity of Exciton States, Phys. Rev. Lett. **111**, 216805 (2013).

[46] T. C. Berkelbach, M. S. Hybertsen, and D. R. Reichman, Theory of neutral and charged excitons in monolayer transition metal dichalcogenides, Phys. Rev. B **88**, 045318 (2013).

[47] B. Scharf, T. Frank, M. Gmitra, J. Fabian, I. Žutić, and V. Perebeinos, Excitonic Stark effect in MoS_2 monolayers, Phys. Rev. B **94**, 245434 (2016).

[48] F. Wu, F. Qu, and A. H. MacDonald, Exciton band structure of monolayer MoS_2, Phys. Rev. B **91**, 075310 (2015).

[49] H.-P. Komsa and A. V. Krasheninnikov, Effects of confinement and environment on the electronic structure and exciton binding

energy of MoS_2 from first principles, Phys. Rev. B **86**, 241201 (2012).

[50] M. M. Ugeda, A. J. Bradley, S.-F. Shi, F. H. da Jornada, Y. Zhang, D. Y. Qiu, W. Ruan, S.-K. Mo, Z. Hussain, Z.-X. Shen, F. Wang, S. G. Louie, and M. F. Crommie, Giant bandgap renormalization and excitonic effects in a monolayer transition metal dichalcogenide semiconductor, Nat. Mat. **13**, 1091 (2014).

[51] A. Raja, A. Chaves, J. Yu, G. Arefe, H. M. Hill, A. F. Rigosi, T. C. Berkelbach, P. Nagler, C. Schüller, T. Korn, C. Nuckolls, J. Hone, L. E. Brus, T. F. Heinz, D. R. Reichman, and A. Chernikov, Coulomb engineering of the bandgap and excitons in two-dimensional materials, Nat. Commun. **8**, 15251 (2017).

[52] A. V. Stier, N. P. Wilson, G. Clark, X. Xu, and S. A. Crooker, Probing the influence of dielectric environment on excitons in monolayer WSe_2: Insight from high magnetic fields, Nano Lett. **16**, 7054 (2016).

[53] W.-T. Hsu, Z.-A. Zhao, L.-J. Li, C.-H. Chen, M.-H. Chiu, P.-S. Chang, Y.-C. Chou, and W.-H. Chang, Second harmonic generation from artificially stacked transition metal dichalcogenide twisted bilayers, ACS Nano **8**, 2951 (2014).

[54] David L. Andrews and William J. Meath, On the role of permanent dipoles in second harmonic generation, J. Phys. B **26**, 4633 (1993).

[55] O. G. Calderon, R. Gutierrez-Castrejon, and J. M. Guerra, High harmonic generation induced by permanent dipole moments, IEEE J. Quantum Electron. **35**, 47 (1999).

[56] O. V. Kibis, G. Y. Slepyan, S. A. Maksimenko, and A. Hoffmann, Matter Coupling to Strong Electromagnetic Fields in Two-Level Quantum Systems with Broken Inversion Symmetry, Phys. Rev. Lett. **102**, 023601 (2009).

[57] L. Tsang, D. Ahn, and S. L. Chuang, Electric field control of optical second-harmonic generation in a quantum well, Appl. Phys. Lett. **52**, 697 (1988).

[58] J. Zhang, M. Ye, S. Bhandari, A. K. M. Muqri, F. Long, S. Bigham, Y. K. Yap, and J. Y. Suh, Enhanced second and third harmonic generations of vertical and planar spiral MoS_2 nanosheets, Nanotech. **28**, 295301 (2017).

[59] R. Wang, H.-C. Chien, J. Kumar, N. Kumar, H.-Y. Chiu, and H. Zhao, Third-harmonic generation in ultrathin films of MoS_2, ACS Appl. Mater. Interfaces **6**, 314 (2014).

[60] R. I. Woodward, R. T. Murray, C. F. Phelan, R. E. P. de Oliveira, T. H. Runcorn, E. J. R. Kelleher, S. Li, E. C. de Oliveira, G. J. M. Fechine, G. Eda, and C. J. S. de Matos, Characterization of the second- and third-order nonlinear optical susceptibilities of monolayer MoS_2 using multiphoton microscopy, 2D Mater. **4**, 011006 (2016).

[61] A. Molina-Sánchez and L. Wirtz, Phonons in single-layer and few-layer MoS_2 and WS_2, Phys. Rev. B **84**, 155413 (2011).